Oil & Gas Science and Technology – Rev. IFP Energies nouvelles **75**, 38 (2020)
© C. Strozzi et al., published by IFP Energies nouvelles, 2020
https://doi.org/10.2516/ogst/2020036

Available online at:
ogst.ifpenergiesnouvelles.fr

Engine Combustion Network – France
Christine Rousselle and Gilles Bruneaux (Guest editors)

REGULAR ARTICLE OPEN ACCESS

Analysis of ECN spray A ignition in a Rapid Compression Machine using simultaneous OH* chemiluminescence and formaldehyde PLIF

Camille Strozzi[1,*], Moez Ben Houidi[2], Julien Sotton[1], and Marc Bellenoue[1]

[1] Institut Pprime, CNRS, Université de Poitiers, ISAE-ENSMA, Département Fluide Thermique Combustion, BP 40109, Teleport 2, 1 avenue Clement Ader, 86962 Futuroscope Chasseneuil-du-Poitou Cedex, France
[2] Clean Combustion Research Center, King Abdullah University of Science and Technology, 23955-6900 Thuwal, Saudi Arabia

Received: 24 December 2019 / Accepted: 12 May 2020

Abstract. The canonical diesel spray A is characterized in an optical Rapid Compression Machine (RCM) at high temperature and density conditions (900 K and 850 K, $\rho = 23$ kg/m^3) using simultaneous high-speed OH* chemiluminescence and two-pulse 355 nm Planar Laser Induced Fluorescence (PLIF). The focus is on the time evolution and the repeatability of the early stages of both cool flame and hot ignition phenomena, and on the time evolution of the fluorescing formaldehyde region in between. In particular, time resolved data related to the cool flame are provided. They show the development of several separated kernels on the spray sides at the onset of formaldehyde appearance. Shortly after this phase, the cool flame region expands at high velocity around the kernels and further downstream towards the richer region at the spray head, reaching finally most of the vapor phase region. The position of the first high temperature kernels and their growth are then characterized, with emphasis on the statistics of their location. These time-resolved data are new and they provide further insights into the dynamics of the spray A ignition. They bring some elements on the underlying mechanisms, which will be useful for the validation and improvement of numerical models devoted to diesel spray ignition.

1 Introduction

One of the main objectives of the Engine Combustion Network (ECN) is to provide robust experimental databases for the analysis of reactive sprays in conditions representative of reciprocating internal combustion engines. These data are particularly relevant for the thorough analysis and understanding of the involved phenomena. They are also crucial for the validation and improvement of accurate numerical models needed for both research and for the design of cleaner and more efficient engines. Spray A is a canonical configuration with a normalized single hole diesel injector operated in well defined initial conditions [1]. It was the subject of numerous investigations (see for instance [2, 3]). In the ECN project, each injector is referenced and can be used on different vessels for more accurate comparisons, taking into account numerous conditions and parameters. For instance, aging effects of each injector can be considered to this purpose [4]. Prior to gathering new measurements for the ECN database, a standardization phase is undertaken for each experimental device in order to ensure the consistency of the data. In particular, the agreement of boundary and initial conditions with the ECN standard are verified, and the characteristics of the spray have to be checked in terms of liquid and vapor penetration, ignition delay and lift-off length. In the framework of the ECN France ANR project, this phase was performed with both existing and new devices [5]. The data obtained from optical Rapid Compression Machines (RCM) and from more classical devices like Constant Volume Preburn (CVP) vessels were successfully compared in this work. The effect of boundary conditions for the different devices was analyzed with special care in Ben Houidi *et al.* [6]. The *Pprime Institute* optical RCM [5, 6] is also employed in the present work: the objective is to characterize and analyze the first instants of the spray A ignition, and in particular the ignition dynamics and its topology. Indeed, despite the large number of studies devoted to the spray A, additional experimental data are still needed to analyze and to better understand the phenomena involved at the early stages of ignition. In particular, there is a lack of time-resolved measurements related to Low Temperature Reactions (LTR). A short overview of the literature is provided in the next paragraph. The collaborative work of Maes *et al.* [7] investigated the spray A behavior before and during the quasi-steady period of the lifted spray flame in different vessels. In particular, formaldehyde formation was identified using single-shot 355 nm Planar Laser Induced Fluorescence (PLIF)

* Corresponding author: camille.strozzi@ensma.fr

This is an Open Access article distributed under the terms of the Creative Commons Attribution License (https://creativecommons.org/licenses/by/4.0), which permits unrestricted use, distribution, and reproduction in any medium, provided the original work is properly cited.

downstream of the liquid length in fuel-rich regions with sufficient entrainment of the high-temperature ambient [8]. The flame structure was also investigated by OH* and single-shot OH PLIF, with a focus on the quasi-steady state period. The spray ignition and in particular the birth of high temperature regions was also monitored by OH* chemiluminescence by Wrigth *et al.* [9], in a *n*-heptane spray. It was generated by a single hole injector in evaporating conditions, e.g. hot air at 800 K, 80 bar. They observed repeatable ignition delays, but reported variability in the location of the OH* kernels (which was also reported in [10, 11] for instance). Wright *et al.* underlined the observed variability of ignition location is consistent with the turbulent nature of the flow: Direct Numerical Simulations (DNS) of turbulent configurations [12, 13] showed hot ignition is located close to the isoline of the most reactive mixture fraction, where the scalar dissipation rate is low. Besides, Wright *et al.* performed Reynolds Averaged Numerical Simulation (RANS) of the same diesel spray experiment: as expected, ignition was located close to the most reactive values of the average mixture fraction. More elements on this topic can be found in [9, 14, 15]. More recently, Tagliante *et al.* [16, 17] studied experimentally and numerically the flame stabilization mechanism in the quasi-steady state spray A using high speed OH chemiluminescence and high frequency 355 nm PLIF. They showed flame propagation and autoignition alternatively participate to the stabilization mechanism. The latter is evidenced by a fast decrease of the formaldehyde lift-off-length, when a kernel autoignites upstream from the flame. The role of autoignition was also reported by Dalakoti *et al.* [18], but it was found secondary in comparison to the flame propagation mechanism. The presence of multibrachial structures similar to that observed in DNS of laminar flames was also reported. In the above studies, the focus was on the flame stabilization mechanism, and the first instants of formaldehyde formation were not characterized in detail. This work was done by Skeen *et al.* [19], who performed simultaneous schlieren and single-shot 355 nm PLIF of spray A ignition (see Fig. 1). The low temperature reactions were visible on schlieren images through a gradient index softening. 355 nm PLIF provided information about intermediate species like formaldehyde, enabling a more accurate characterization of the topology of regions affected by low temperature reactions. Furthermore, the low temperature reactions could be detected earlier with this technique. In this study, the PLIF measurements were not time-resolved and several combustion events were needed to analyze the dynamics of ignition. The authors reported CH_2O first appears as lobes at the radial periphery downstream of the liquid length behind the penetrating jet head, and then it reaches the spray head. The authors assumed this might result of the rapid convective mixing from the lobes of formaldehyde to the core of the jet. The authors also reported the high temperature ignition appears later in the formaldehyde region, and it was described as a fast and volumetric process. The low temperature flame propagation was studied and modeled by Dahms *et al.* [20], who proposed the concept of turbulent cool flame wave. The group of authors used a Lagrangian flamelet approach with

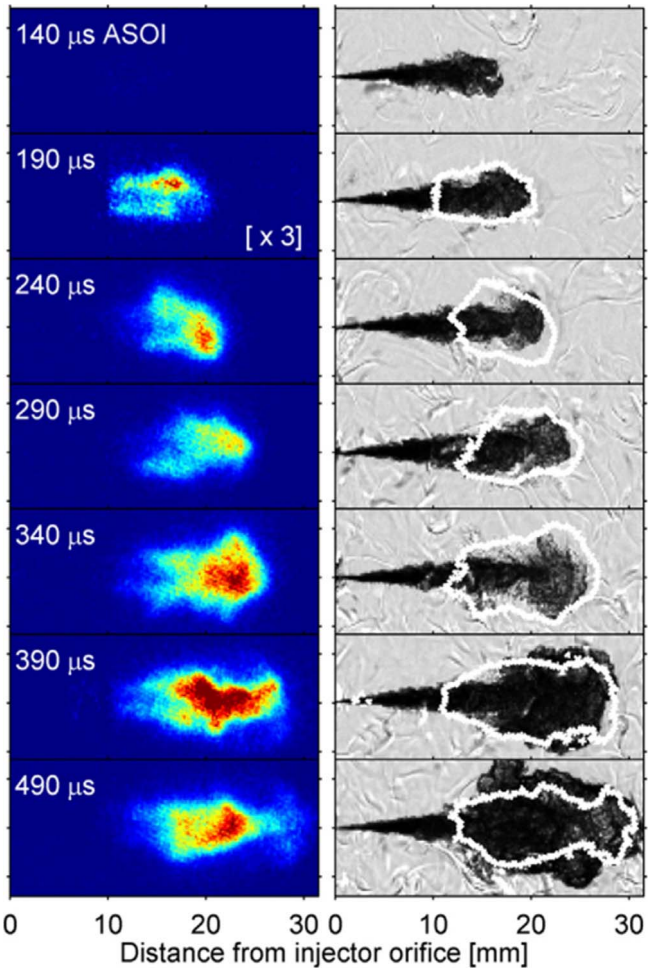

Fig. 1. Time sequence of 355 nm PLIF (left) and schlieren images (right) for spray A. Reprinted from Skeen *et al.* [19] with permission of *Elsevier*.

detailed chemistry. They suggested the scalar dissipation plays a crucial role in the cool flame propagation, e.g. the heat and species turbulent transport provides a significant contribution to the propagation from the first lobes towards the richer and colder head of the jet. The authors suggested, using homogeneous reactor calculations, that without this turbulence chemistry interaction, low temperature reaction would have occurred significantly later in this region. They also reported there is a period, between the end of the cool flame process and the beginning of high temperature reactions, when formaldehyde is formed in most of the vapor region.

The dynamics of the cool flame during ignition was also investigated in the case of non-premixed flames. Krisman *et al.* [21] studied numerically the ignition process of a laminar mixing layer of DiMethylEther (DME) with hot air coflow. With increasing oxidizer temperatures, a transition from flame structures driven by heat and species diffusion to autoignition fronts is reported. For an intermediate value of 900 K, the authors put into evidence tetrabrachial structures, with branches related to the contributions of either

diffusive or autoignitive processes. At this temperature, autoignition contributes significantly to the flame stabilization. The work was extended towards turbulent and high pressure conditions representative of diesel engines. These 2D DNS computations are performed with air at 900 K and DME at 400 K, and $P = 40$ bar [22]. In this study, low temperature ignition is first initiated in lean regions, and then the cool flame propagates towards richer regions, with a velocity higher than expected based on the gradient of the first stage autoignition delay in homogeneous reactors. The high temperature ignition starts close to the stoichiometric line, with a delay shorter than in the case of a homogeneous reactor. More recently, Borghesi *et al.* [23] performed 3D Direct Numerical Simulation (DNS) of a jet of *n*-dodecane and hot diluted air undergoing autoignition. The problem was idealized in comparison to the diphasic and unsteady spray A, but the conditions were representative of this diesel spray. The authors evidenced the presence of multiple cool flame kernels in nearly stoichiometric zones propagating at high velocity towards richer zones. The impact of these low temperature reactions on high temperature ignition is also investigated: high temperature kernels appear in rich regions, expand, and then they propagate following the stoichiometric iso-surface.

Finally, Krisman *et al.* [24] performed parametric studies using 2D DNS computations in different cases around the baseline spray A conditions. The time evolution of the different combustion modes was analyzed for different oxidizer temperatures (800 K, 900 K, and 1100 K), oxygen molar fraction (12%, 15%, and 21% O_2), turbulence and premixedness of the fuel stream. The results showed low temperature ignition mostly starts in lean mixture – except at 1100 K, it is moved to rich conditions – then the cool flame propagates from lean towards richer mixtures through diffusive processes. High temperature ignition essentially occurs in premixed rich conditions, except for 21% O_2, where hot ignition occurs closer to the stoichiometry. Then non-premixed combustion occurs, propagating towards richer and leaner mixtures until reaching the stoichiometric line. The authors also highlighted the cool flame behavior strongly affects the location and time of hot ignition (see also [25]). This phenomenology is in agreement with the findings of both Dahms *et al.* [20] and Borghesi *et al.* [23].

The literature survey above shows the significant role of low temperature reactions on the high temperature ignition process in the spray A conditions, and more generally on the ignition of non-premixed turbulent flames with hot co-flows. It also evidences a lack of experimental data regarding the time-evolution of CH_2O at early stages of the spray A ignition. In this respect, the present work provides temporal measurements for this reference combustion experiment, with a focus on the early stages of the cool flame and of the hot ignition phenomenon. In particular, new experimental data are gathered regarding the temporal evolution of CH_2O region before hot ignition, while higher temperature reactions are monitored by analyzing OH* chemiluminescence emissions. To this purpose, high-speed OH* chemiluminescence and two-pulse 355 nm PLIF imaging are employed simultaneously in the optical RCM of *Pprime Institute*. This two-pulse PLIF technique was recently employed by Strozzi *et al.* [26], in order to analyze the propagation of both the cool flame and hot ignition in lean premixed conditions representative of SICI and HCCI engines.

The manuscript is structured as follows: after a short description of the device, the evolution of formaldehyde fields is analyzed at 900 K and 850 K, as well as their reproducibility. The early stages of OH* emission are then considered, with emphasis on the location of the first high temperature kernels and on their propagation leading to the flame stabilization.

2 Experimental setup

2.1 The RCM in spray A configuration

The optical RCM of *Pprime Institute* features a square piston with rounded corners, and a 420 mm compression stroke. For a given compression ratio, these features enable large optical accesses at visible and UV wavelengths. In this work, the ECN injector (#306, 14) is mounted on the cylinder head, and injection is made on the cylinder axis. At the end of compression, dead volume geometry is close to a cube with 50 mm edges. Optical accesses of 50×50 mm^2 are perpendicular to the cylinder axis. The spray is injected on the cylinder axis. The RCM and its qualification for ECN spray A is described in Hespel *et al.* [5], and boundary conditions and their influence were characterized in detail in Ben Houidi *et al.* [6].

Injection is triggered 74 ms after the end of compression, for a duration of 2.6 ms (command duration of 1.5 ms), when low velocity and appropriate temperature conditions are obtained. Figure 2 reports the corresponding pressure traces in the reactive case and in inert conditions, with and without injection. They highlight the effects of vaporization and heat release in this confined environment, the reader is referred to Ben Houidi *et al.* [6] for more information. Two different temperatures at the Start Of Injection

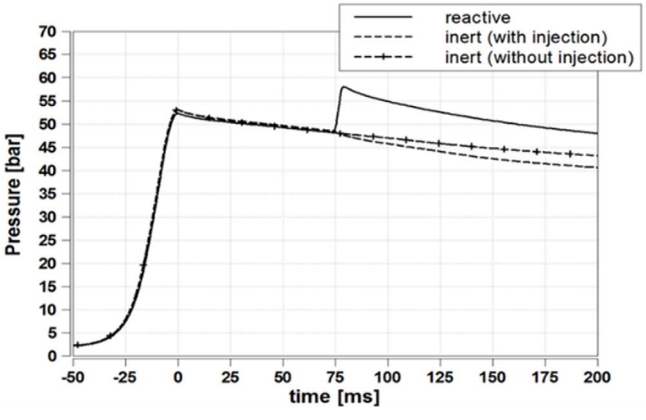

Fig. 2. Pressure traces measured during spray A experiments in inert and reactive conditions. Reprinted from Ben Houidi *et al.* [6] with the permission of *OGST*, *IFPEN*.

Table 1. Summary of the RCM settings at ECN spray A target conditions.

Compression ratio	9 (lowest, volume after compression = 131 cm^3)	
Temperature before compression	363 K	
Gas composition	– Reactive: O_2/N_2/Ar 15/40/45% mol	– Reactive: O_2/N_2/Ar 15/55/30% mol
Average (bulk) density at SOI	23 ± 0.2 kg/m^3	23.2 ± 0.1 kg/m^3
Core density at SOI (ρ_{inj})	21.3 kg/m^3	21.6 ± 0.1 kg/m^3
Injector #	14	
Injection timing (t_{inj})	74 ms after the end of compression	
Pressure at t_{inj}	47.84 ± 0.43 bar	48.06 ± 0.1 bar
Temperature at t_{inj}	– Target temperature: T_{inj} = 900 K. – Adiabatic core temperature T_c = 939 ± 2 K. – Time averaged temperature at chamber center at t_{inj} ± 50 ms: T_{core_center} = 917 ± 8 K. – Space averaged core temperature at t_{inj}: T_{core} = 925 ± 18 K.	– Target temperature: T_{inj} = 850 K. – Adiabatic core temperature T_c = 884 K. – Time averaged temperature at chamber center at t_{inj} ± 50 ms: T_{core_center} = 860 ± 17 K.

(SOI) are targeted herein: 850 K and 900 K. Initial temperature and volumetric compression ratio are kept constant, and temperature at injection timing is varied by changing the diluent gas composition (see Tab. 1). Core temperature is measured using 7.6 µm thermocouples following two different approaches: T_{core_center} represents the temperature measured at the center of the chamber, e.g. on the injector axis, at 23 mm from the injector tip. This value is obtained by averaging the temperature signal over a time window of ±50 ms centered on the injection timing, these values are averaged over three repeated tests. T_{core} represents the spatial average measured in the core at the injection timing. It is based on 10 thermocouple positions and five repeated tests at SOI times [5]. For the target condition T_{inj} = 900 K, these two approaches lead to very close values: the difference between T_{core_center} and T_{core} is equal to 8 K (see Tab. 1). Oxygen molar fraction is set to 15% according to the ECN spray A standards. Additional information is reported in this table. For more details regarding the RCM and the injection system, the reader is referred to Hespel *et al.* [5].

2.2 Optical setup

OH* chemiluminescence and 355 nm PLIF are used simultaneously during spray A ignition. The PLIF camera axis is perpendicular to the window (see Fig. 3). It is also normal to the cylinder axis. Chemiluminescence is recorded through the same window and the axes of the two cameras form an angle of 10°.

OH* chemiluminescence is detected using a fast camera *Photron* SA-5 recording at 46.5 kHz coupled to a *Hamamatsu* C10880 intensifier with a 10 µs gate. It is fitted with a 94 mm *Cerco* UV lens. A bandpass filter centered on 310 nm with a Full Width at Half Maximum (FWHM) of 10 nm is used to isolate the OH* contribution from the rest of the flame emission (*Asahi Spectra* ZBPA310).

The PLIF setup is the following: a double cavity Nd:YAG laser provides two-pulse excitation using its third harmonics at 355 nm. An energy ranging from 90 mJ to 120 mJ is released over each pulse duration of 6 ns. The thickness of the laser sheet is 300 µm. This value is representative of the effective resolution of fluorescence images, it corresponds to approximately six pixels. Fluorescence signal is recorded using a double frame intensified CCD camera (PI-MAX 4, *Princeton Instruments*). The gate time is ranging from 100 ns to 250 ns. The camera is fitted with a 105 mm UV nikkor lens and a bandpass filter centered on 445 nm with a FWHM of 49.5 nm (*Semrock* 445/45). This filter has a high transmission level in a significant part of the formaldehyde fluorescence emission spectra. It removes as well the elastic contribution issued from the laser, except in the liquid part of the spray where a contribution of scattered light is still observed. One has to note that Polycyclic Aromatic Hydrocarbon (PAH) molecules are excited as well at this wavelength, but they are temporally and spatially separated from formaldehyde in the spray A [19]. As this work focuses on the early stages of spray A ignition, 355 nm excited fluorescence signal corresponds to formaldehyde [19]. This point is further discussed in the next section. In this study, emphasis is on the time evolution of CH_2O fields, and therefore couples of images separated by 20–100 µs are recorded using this two-pulse PLIF setup. In order to ensure an appropriate phasing of the images, the laser and the PI-MAX camera are triggered with respect

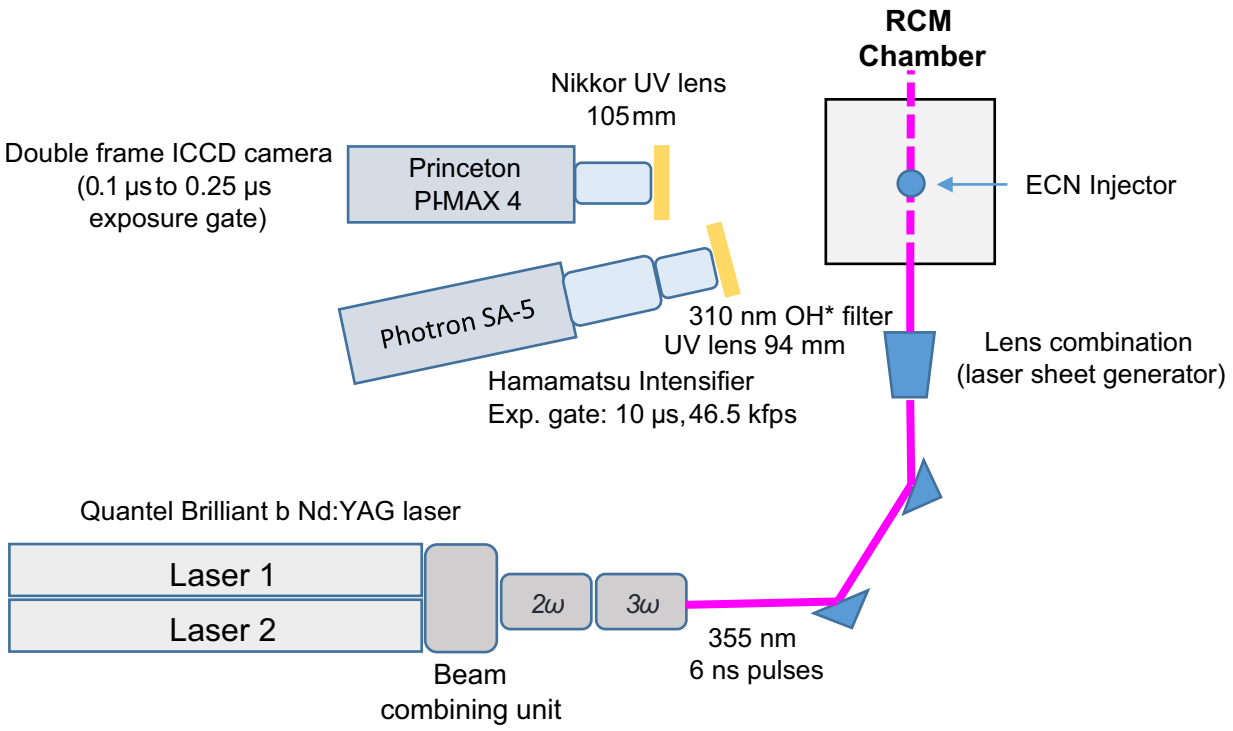

Fig. 3. Optical set-up for simultaneous OH* chemiluminescence and two-pulse 355 nm PLIF of spray A in the RCM.

to the command of injection. For convenience, the reference number of each experiment is reported in the upper left corner of the first image recorded by the double frame camera.

3 Experimental results

3.1 Overview of the time sequence of spray A ignition

Figure 4 describes the time sequence of spray A ignition at 900 K, as observed using OH* chemiluminescence and 355 nm PLIF. The injection trigger signal is sent 74 ms after the end of compression. Due to the hydraulic delay, injection starts 336 ± 10 µs after the injection trigger. CH_2O is then detected about 264 µs After the Start Of Injection (ASOI), e.g. 600 µs after the trigger signal of injection. The first OH* kernels appear at about 500 µs ASOI. The standard deviation of ignition delay is 30 µs in the 900 K condition investigated herein [5]. At this instant, formaldehyde is consumed by high temperature reactions. Later, PAH may be formed and contribute to fluorescence signal, which is discussed in the next section. Injection stops at about 2.6 ms ASOI. The corresponding pressure trace is reported in Figure 2. The heat release induced by spray ignition is clearly evidenced and results from the confined conditions.

3.2 Focus on cool flame ignition

3.2.1 Interpretation of PLIF images

Dynamics of the first stages of spray ignition is first investigated using PLIF with excitation at 355 nm, for two different target temperatures of 900 K and 850 K. At these early instants, the fluorescence signal is issued from formaldehyde, which is produced by low temperature reactions, e.g. by the cool flame. Similarly as in Maes *et al.* [7], some signal upstream on the axis is due to elastic contribution at $y \leq 12$ mm at 900 K (respectively $y \leq 15$ mm at 850 K) (see the white arrow in Fig. 5). It is not totally suppressed by the filters. The rest of the image is interpreted as formaldehyde signal in the investigated time range. No fluorescence signal issued from the fuel was observed in reactive conditions, e.g. in the presence of oxygen. At late instants, when high temperature reactions dominate, PAH molecules can be formed. They are also excited at this wavelength and emit fluorescence signal close to the extremity of the spray, in a region that is generally separated from that of formaldehyde in instantaneous images [19]. The presence of PAH is not observed in the 355 nm PLIF images reported below, as the study focuses on the early stages of the spray development. For a review of the fluorescence excitations schemes of CH_2O in spray A conditions, the reader is referred to Bakker *et al.* [27]).

3.2.2 Two-pulse 355 nm PLIF at 900 K

Figure 5 reports couples of instantaneous images recorded during several compression ignition experiments. Each couple highlighted by a double head blue arrow corresponds to the same ignition event. A median and a Gaussian filter of five pixels size are successively applied to remove measurement noise. Images are thresholded to remove background signal, as shown by the colorbar. At the left bottom of Figure 5, a mask is used on two images, where the laser

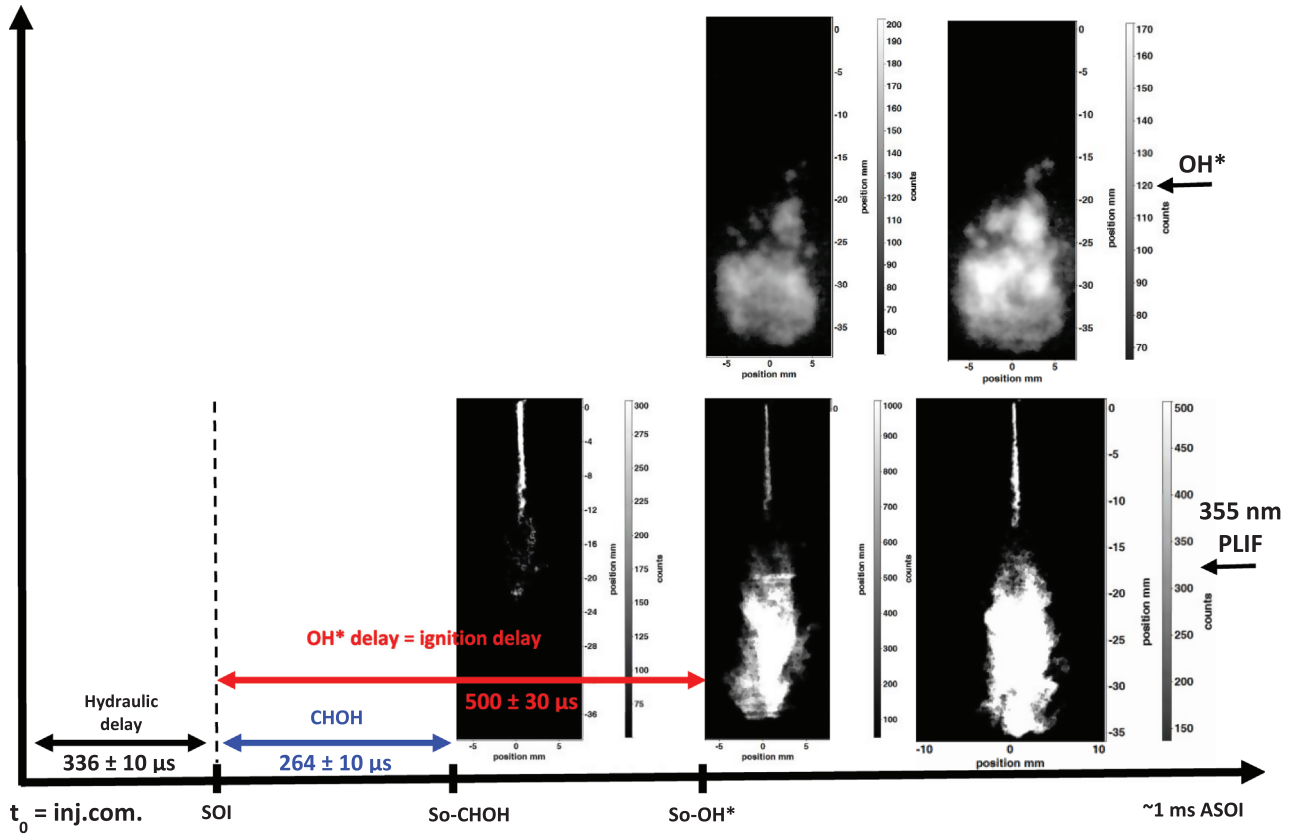

Fig. 4. Time sequence of the spray A autoignition.

sheet does not excite the region located between 0 mm and 13 mm from the injector tip. First images of formaldehyde were obtained at 264 µs ASOI. At this instant, several pockets of formaldehyde are located on the sides of the spray, see the region labelled A for instance. Formaldehyde is absent on the spray axis as the mixture is rich in this region, leading to a larger cool flame ignition delay [8, 20]. A similar topology is observed 20 µs later, with the growth of one of the kernels and the extension of the tip of formaldehyde region further downstream the injector. This zone is labelled as region B in Figure 5. Unlike previous studies [19], this work evidences multiple separate kernels – labelled 1–3 – at the onset of CH_2O appearance. Furthermore, time evolution of these CH_2O regions was not resolved before, as most studies on the subject used single-shot PLIF and because a very short delay of 20 µs can be used here. The same trend is observed at 314 µs ASOI. The formaldehyde tip further propagates downstream up to 464 µs ASOI, however from $t = 364$ µs ASOI, the topology of PLIF images changes: cool flame also occurred on the axis, and formaldehyde occupies a single region delineated by sharp contours. The couple of images obtained during the same experiment at 314 µs and 364 µs show the fluorescent zone propagates, but its global shape is conserved. In particular, the same asymmetric structures are formed on the spray sides, labelled as C and D, where formaldehyde is being mixed with the surrounding region. This confirms formaldehyde is formed in all the vapor phase at these instants (as suggested in [20]), except close to the injector tip, where the residence time of the vapor is shorter. The last two images are also recorded during the same experiment: they show formaldehyde disappear at 564 µs ASOI as a result of hot ignition, downstream and on the sides of the spray, as shown by the red circles. This is consistent with the appearance of OH* at these instants and at a close location (see the red circles in Fig. 6). Similar images are obtained when the spray is fully stabilized at $t \sim 1$ ms ASOI: Figure 4 shows the fluorescence zone ends at the same position, e.g. at $y = 35$ mm from injector tip. Reynolds averaged fluorescence fields shown in Figure 7 display trends similar to the instantaneous images reported in Figure 5. Please note the average is slightly affected by a difference of laser sheet position at $2 < y < 14$ mm at 264 µs ASOI. Despite the number of experiment is not sufficient to reach the full convergence, the figure illustrates the experiments are consistent with the axisymmetric shapes typically obtained from URANS computations [28, 29]. In particular, this figure displays at 364 µs a hollow zone without formaldehyde just downstream of the liquid length in the rich mixture located on the spray axis – labelled as region E – and a quasi-hemispherical jet at the opposite extremity.

Repeatability of formaldehyde fields is analyzed at the onset of cool flame development, e.g. for couples of images at 264 µs and 364 µs ASOI (see Fig. 8). On the first images, several kernels of formaldehyde are more or less developed on the spray sides. The lack of formaldehyde observed on the spray axis at 264 µs – labelled as F – is consistent with the LES temperature field reported by Pei *et al.* at

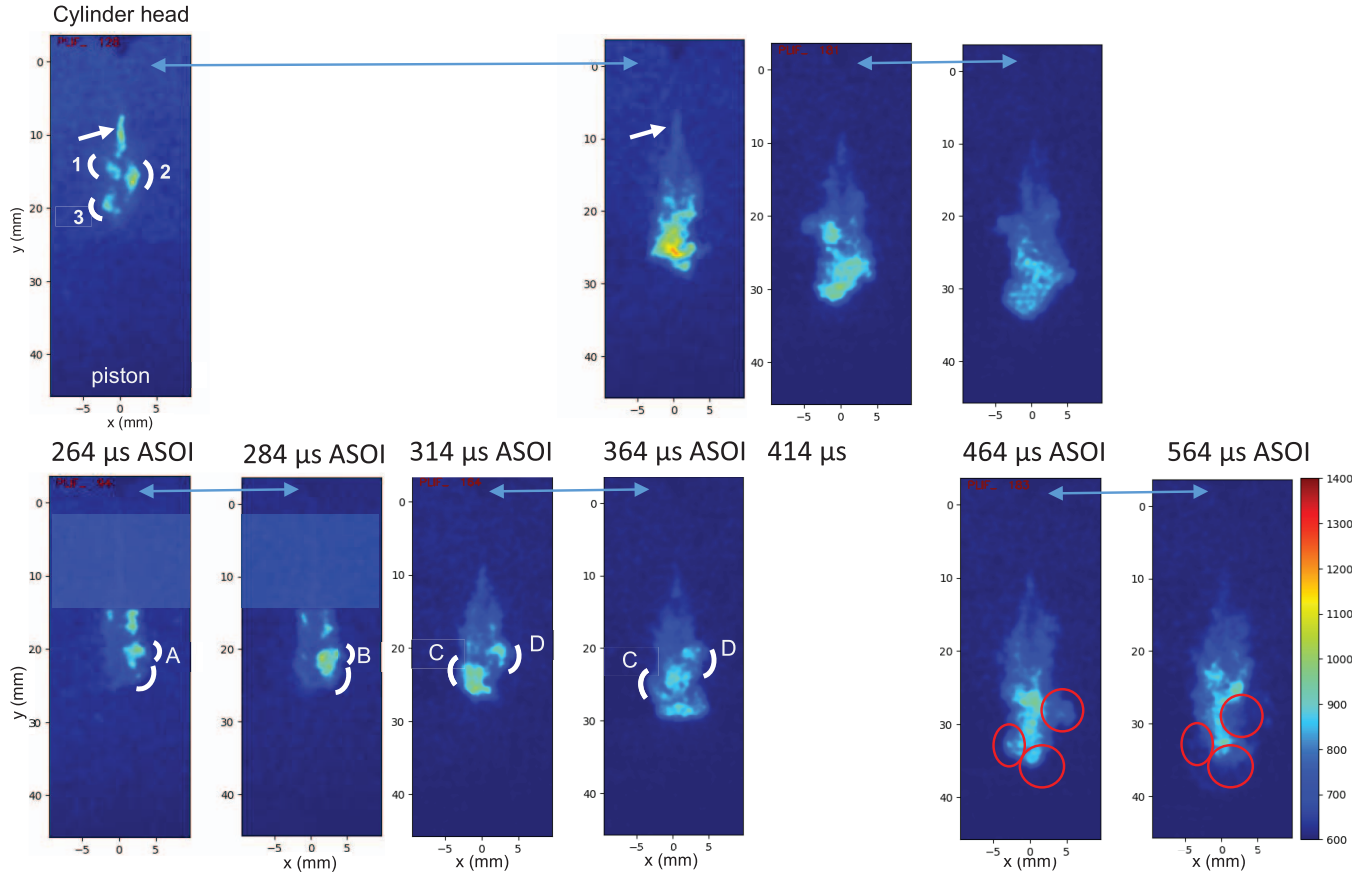

Fig. 5. Time evolution of two-pulse formaldehyde PLIF images during spray A autoignition at $T_{inj} = 900$ K, $\rho_{inj} = 21.3$ kg/m^3. Couples of images emphasized with blue arrows correspond to the same autoignition experiment.

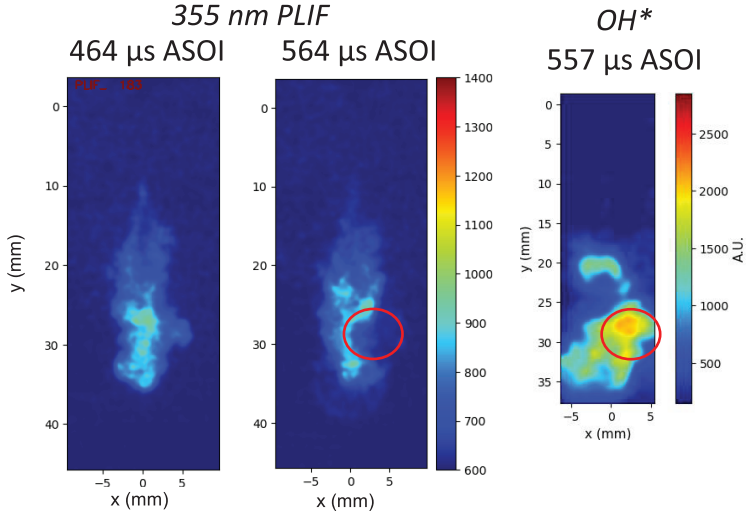

Fig. 6. Three hundred and fifty five nanometers PLIF images before (left) and after (middle) the onset of high temperature reactions. The corresponding OH* image is reported on the right. Experimental conditions: $T_{inj} = 900$ K, $\rho_{inj} = 21.3$ kg/m^3.

$t = 320$ µs ASOI, e.g. during the first stage of ignition [29]. This results from the high fuel equivalence ratio in this region. This is also consistent with the phenomenology gathered from DNS studies [23, 24], where low temperature reactions first initiate in lean or nearly stoichiometric regions and then propagate towards richer locations. In the present work, moderate shot-to-shot variations exist, as a result of the hydraulic delay scatter (±10 µs). This is

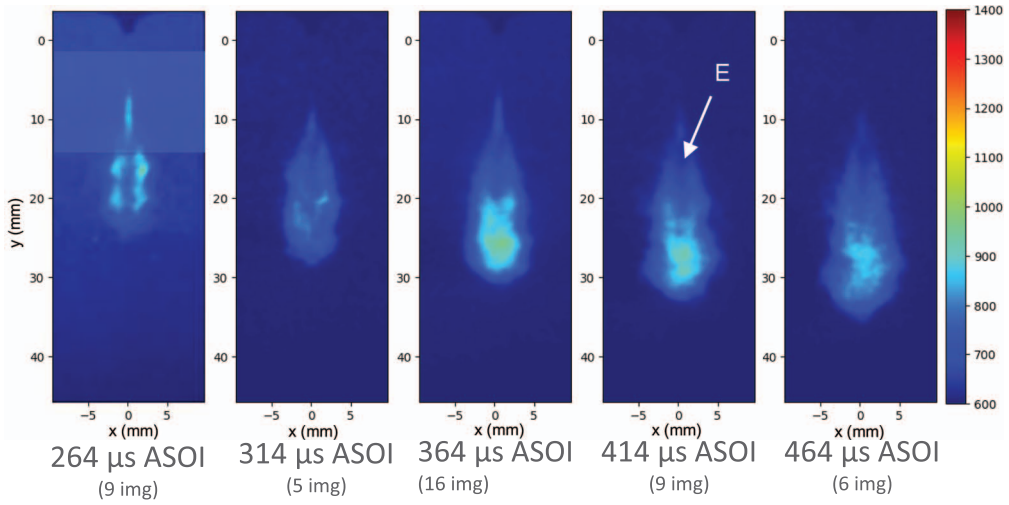

Fig. 7. Averaged images of formaldehyde PLIF images at $T_{\text{inj}} = 900$ K, $\rho_{\text{inj}} = 21.3$ kg/m^3, at different instants. Each averaged field is based on 6–16 experiments.

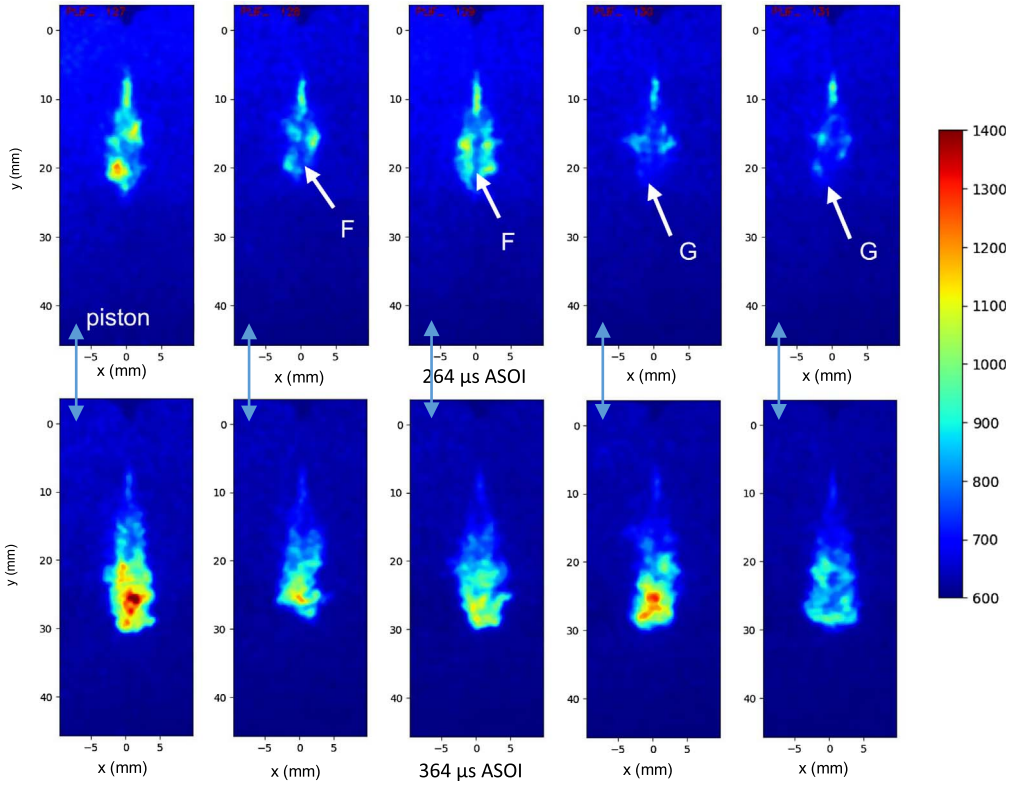

Fig. 8. Formaldehyde PLIF images during spray A autoignition at $T_{\text{inj}} = 900$ K, $\rho_{\text{inj}} = 21.3$ kg/m^3, at $t = 264$ µs and 364 µs ASOI. Images emphasized with blue arrows correspond to the same autoignition experiment.

consistent with the fact experiments featuring the most developed formaldehyde lobes at 264 µs (e.g., exp. #127 and #129, respectively on the left and the middle) also feature a higher formaldehyde penetration at 364 µs. Another point that has to be underlined in this Figure 8, is that the first image of experiments 130 and 131 features very low signal of formaldehyde downstream, as shown by label G at $18 < y < 22$ mm from the injector tip. This suggests cool flame has just started at this location. By contrast, the level is higher on other images at the same instant. This highlights in that case the higher progress of the cool flame phenomenon. This suggests sequential autoignition occurs at the onset of cool flame at 264 µs: the cool flame front is propagating downstream inside the vapor, while the vapor

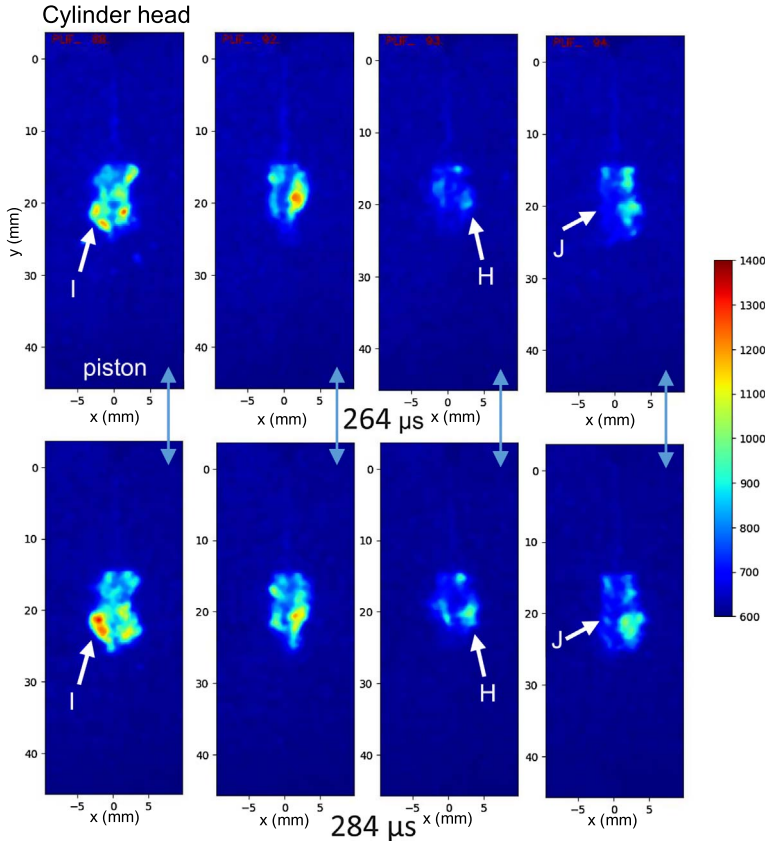

Fig. 9. Formaldehyde PLIF images during spray A autoignition at $T_{inj} = 900$ K, $\rho_{inj} = 21.3$ kg/m^3, at $t = 264$ µs and 284 µs ASOI. Images emphasized with blue arrows correspond to the same autoignition experiment.

tip is starting to react. This point is further discussed at the end of the section. One hundred microseconds later, formaldehyde seems to be formed in the whole vapor phase, a behavior reported by Dahms *et al.* [20]. This formaldehyde region is convected downwards along the spray axis, following the vapor dynamics. This formaldehyde penetration is investigated in more details below.

Additional formaldehyde fields measured during four experiments are reported in Figure 9 with a shorter delay dt = 20 µs between consecutive images. They confirm the existence of several formaldehyde kernels, which are expanding – label H – and/or increasing in fluorescence intensity (see for instance label I). Other kernels may appear – at least in the measurement plane – as shown by label J. The left two images also feature a fast propagation of the formaldehyde in the vapor region, and in particular downstream, close to the spray head. These images also confirm there is variability in the position of the kernels, which is assumed to result from heterogeneities – in particular of equivalence ratio – induced by the large scale turbulent structures on the spray sides. Some variability in the position of the downstream extremity of formaldehyde is also observed, and it seems to be affected by the turbulent flow as well.

In order to confirm this analysis, Figure 10 reports in blue line the evolution of Vapor Penetration (VP) as obtained from schlieren imaging using the standard ECN algorithm [5, 30]. It is not measured simultaneously to the CH_2O/OH* records displayed above. Penetration of formaldehyde is reported as well in this figure *versus* time: after filtering and binarizing formaldehyde PLIF images, CH_2O penetration is calculated by detecting the highest value of the y coordinate of the binarized formaldehyde region.

For these two-pulse PLIF experiments, penetrations obtained from the first image are reported in Figure 10 with blue dots, and violet hollow circles are used for the second image of the two-pulse diagnosis. Polynomial fits are reported in dotted and dashed lines, and similar results are obtained for the two images. A good agreement is observed between the vapor penetration – blue solid line – and formaldehyde vapor penetration. This formaldehyde penetration is lower than that of vapor at the first instants. This trend is reversed from 364 µs, suggesting an acceleration of formaldehyde region. The fact formaldehyde penetration is slightly higher than vapor penetration is due to the CH_2O penetration processing method, which tends to overestimate penetration in comparison to the standard ECN vapor penetration post-processing. It is worth noticing the double pulse system enables calculating formaldehyde penetration velocities of single experiments: in that case, penetration velocity values are neither biased by shot-to-shot fluctuations of the reactive flow, and nor affected by the scatter of hydraulic delay (even if it affects the instant corresponding to the velocity value). The instantaneous velocity values are reported with orange dots, and the average values are reported in orange solid line. The average

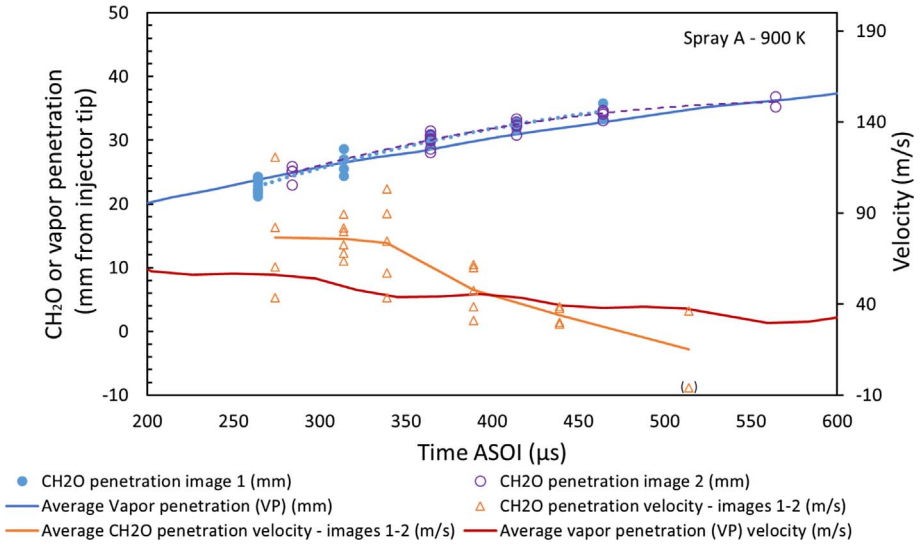

Fig. 10. Formaldehyde and vapour penetrations at $T_{inj} = 900$ K, $\rho_{inj} = 21.3$ kg/m^3 (blue and violet), and corresponding penetration velocities (orange and red).

values of vapor penetration velocity are reported with a red line.

Three hundred and ninety microseconds after SOI and later, formaldehyde penetration velocity is close to that of vapor, confirming formaldehyde is formed in all the vapor phase during this period. Then it becomes negative when the hot ignition starts, as high temperature reactions consume formaldehyde.

It is worth noticing that in the early stages of low temperature ignition, between 264 µs and 364 µs, the average penetration velocity is significantly higher for CH_2O than for vapor. This confirms the cool flame propagates inside the vapor. The average propagation velocity ranges from 6 m/s to 8 m/s, with instantaneous values reaching up to 18 m/s. This apparent propagation involves a part of sequential autoignition: it is starting from the first ignition kernels and continues downstream in the vapor. Borghesi *et al.* suggested in a similar configuration that diffusion contributes as well to the propagation [23]. They showed the coexistence of both autoignitive and diffusively controlled cool flame fronts, the propagation mode being correlated to the local mixture fraction. The contribution of diffusion to cool flame propagation was also highlighted in Krisman *et al.* [24]. Dahms *et al.* [20] referred to this phase as a "turbulent cool flame wave". As stated above, very low levels of formaldehyde exist downstream in some of our PLIF images, see the G labels in Figure 8 at $t = 264$ µs ASOI. This just highlights the fact the time scale related to cool flame reactions (LTR excitation time) is not negligible in comparison to that of the cool flame penetration: when the cool flame has occurred in the upstream kernels, it is only starting downstream at the vapor extremity. This element does not confirm or infirm the role of turbulent transport in the cool flame propagation suggested by Dahms *et al.* Nevertheless, it is clear fuel stratification affects the cool flame wave propagation in the vapor at these instants. Besides, fuel stratification is also expected to drive the first stages of the growth of formaldehyde kernels. The cool flame propagation phenomenon was mentioned in other studies [25, 26, 31, 32], and also in DNS of jets of different fuels in hot oxidizer environment [21–24], eventually in canonical configurations directly related to spray A ignition. Our observations present similarities with the phenomenology described in these works, at the first instants of low temperature ignition: several low temperature kernels form in a leaner region on the spray sides and propagate fast towards richer regions. In our case, this region corresponds to the richer spray head. This is consistent with the LES mixture fraction field of Pei *et al.* at 320 µs ASOI [29], where the spray sides feature leaner mixture regions compared to the spray head. In comparison to previous experimental studies, the results reported in the present work provide more information and time resolution on the first instants of the low temperature ignition process. They confirm the existence of cool flame wave propagation, as suggested by Dahms *et al.* [20]. To the authors' knowledge, time resolved PLIF images of cool flame propagation in the early stages of spray A ignition are reported for the first time, which will be useful for the validation of numerical models at the early stages of spray ignition.

3.2.3 Two-pulse 355 nm PLIF at 850 K

Figure 11 displays couples of instantaneous images obtained with several compression ignition experiments at 850 K, for similar core densities $\rho_{inj} = 21.6$ kg/m^3. Similar to PLIF images at 900 K, formaldehyde is first observed on the lobes located aside from the spray axis. At this lower temperature, this corresponds to 364 µs ASOI. This topology is still observed 50 µs later. At 464 µS ASOI, formaldehyde is formed in the whole vapor zone and fluorescence levels increase with time until 614 µs ASOI. One hundred microseconds later during the same experiment, formaldehyde is consumed by higher temperature reactions close to the

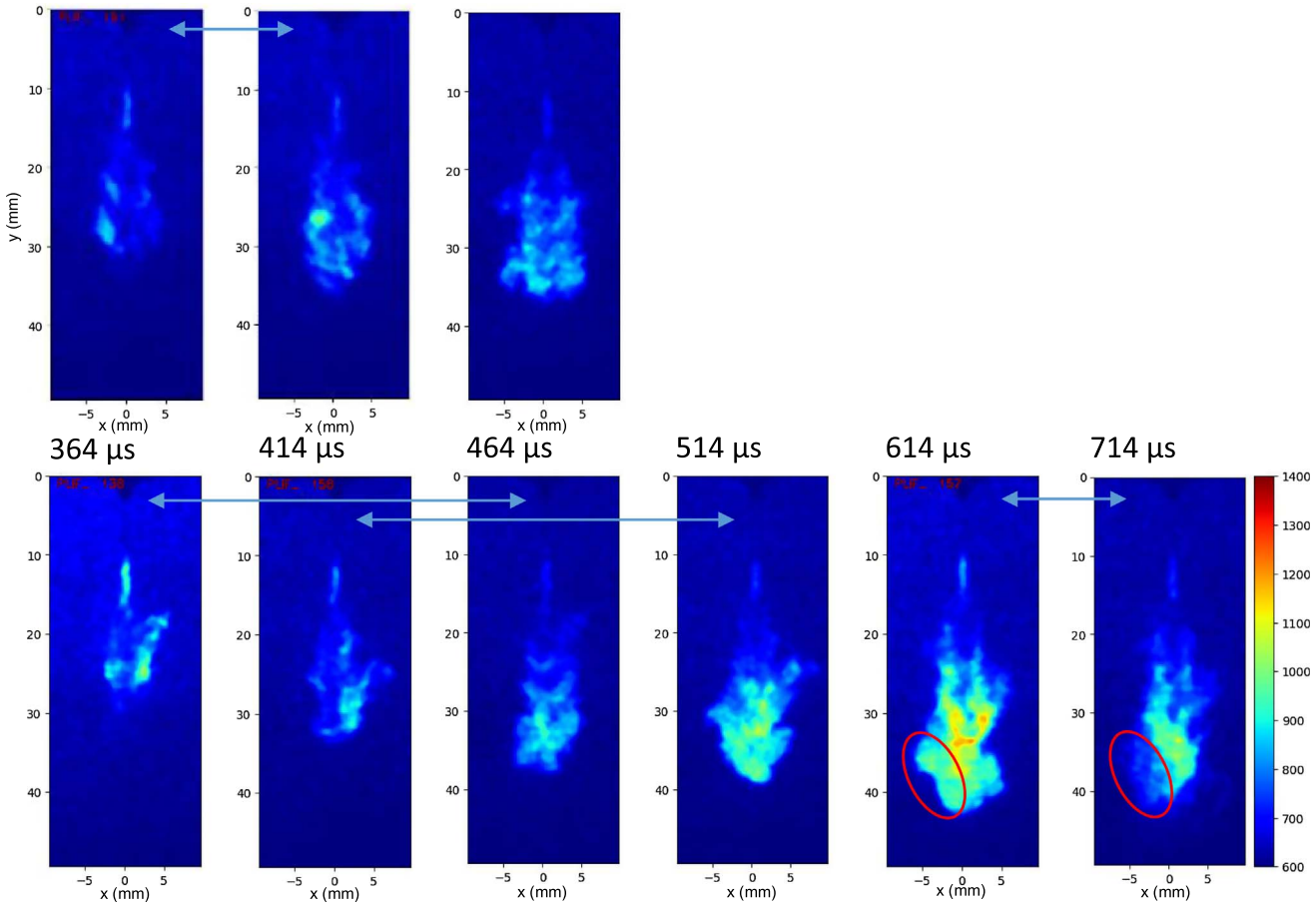

Fig. 11. Time evolution of two-pulse formaldehyde PLIF images during spray A autoignition at $T_{inj} = 850$ K, $\rho_{inj} = 21.6$ kg/m^3. Couples of images emphasized with arrows correspond to the same autoignition experiment.

extremity of the "jet". This region is highlighted by red circles. Besides, OH* is also observed at this instant downstream at the jet extremity. In comparison to 900 K, formaldehyde region is wider and larger scales are observed in the flow: as the cool flame and hot ignition occur later at 850 K, the vapor jet has more time to develop before ignition occurs.

Figure 12 reports formaldehyde penetrations and the corresponding velocities at 850 K. If the penetration lengths are larger than at 900 K on average, the phenomenology is similar: formaldehyde propagates fast at the very early stages of the spray ignition, as a result the sequential appearance of the cool flame in the vapor zone. Formaldehyde penetration velocity was not measured in the intermediate period when formaldehyde is formed in the whole vapor region. Nevertheless, the negative velocity value measured later at 664 µs shows formaldehyde is consumed, as a result of the high temperature reactions at the extremity of the jet during hot ignition.

3.3 Focus on hot ignition: OH* chemiluminescence

Figure 13 displays instantaneous chemiluminescence images of an ignition event at 900 K, and core density $\rho_{inj} = 21.3$ kg/m^3. OH* images are filtered with the same procedure as described above for instantaneous formaldehyde PLIF images. The first occurrence of OH* radical, which is involved in high temperature reactions, is shown in this figure as a small kernel of about 2 mm diameter at $t = 470$ µs ASOI. The existence of very small kernels was also reported in the 2D DNS study of Krisman *et al.* [24]. The position of the first OH* kernel varies from experiment to experiment, but it remains mostly located in the lower part of the image, in the vapor ($x < 35$ mm). At this period, formaldehyde was present in the whole vapor region. On the second OH* image, the kernel has developed radially, with a high apparent velocity: a magnitude order of 100 m/s is estimated based on a 1D spherical growth assumption. This value is significantly higher than that of laminar burning velocities on the burned gas side $S_b°$. By contrast, flamelets propagation velocities in unburned mixture ranging from $0.6S_L$–$1.2S_L$ were observed in autoignition of non-premixed flames [33]. This suggests autoignition phenomenon still provides an important contribution to the kernel growth in the present case. The growth of the first kernel can vary from experiment to experiment: in some cases, the apparent velocity is closer to a few tens of meters per second, and consequently the role of autoignition in the first kernel growth is less important. On the same image, one can observe other kernels

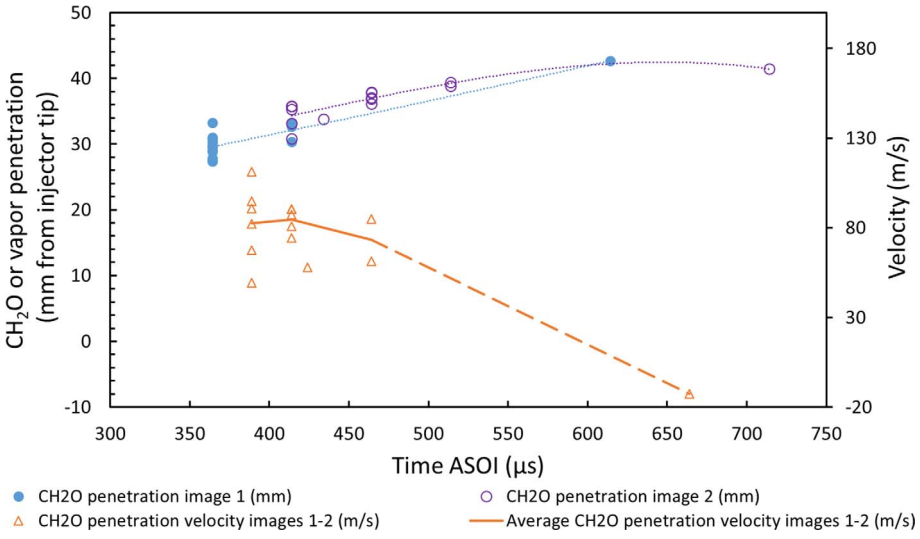

Fig. 12. Formaldehyde penetration at $T_{inj} = 850$ K, $\rho_{inj} = 21.6$ kg/m^3 (blue and violet). Formaldehyde penetration velocity (orange).

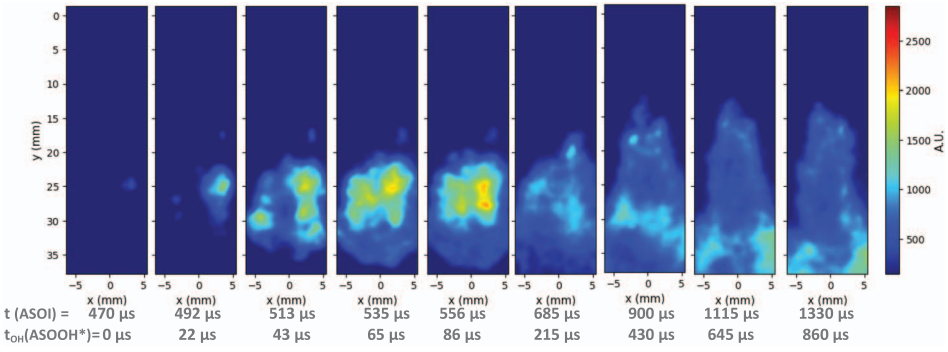

Fig. 13. Filtered instantaneous OH* images during a spray A autoignition experiment at $T_{inj} = 900$ K, $\rho_{inj} = 21.3$ kg/m^3.

appear at some distance of the first one. Later, a large OH* region exists at $t = 513$ µs ASOI, and then it further propagates into the vapor, both downstream and towards the injector tip. The flame is stabilized about 300 µs later: the lift-off length reaches approximately 14 mm between 900 µs and 1330 µs. The flame is stabilized by two different mechanisms: deflagration and autoignition, which is in agreement with Tagliante *et al.* [16]. In particular, autoignition can lead to the formation of hot kernels isolated in the vapor upstream from the main flame as shown by Figure A1 (Appendix). This leads to a sharp decrease of the instantaneous lift-off length [16].

A global point of view is provided by the averaged OH* fields (see Fig. 14). They are issued from 51 experiments performed at 900 K. Prior to the averaging process, images were phased from $t = 0$ µs ASOOH*, which corresponds to the instant when the first OH* ignition kernel is observed. Considering the number of total experiments, it was not found necessary to filter OH* images and Figure 14 reports the average of raw images. This figure provides a clear view of the average propagation of OH* at the both extremities of this hot ignition region. One can remark the intensity reaches a local maximum at $t = 86$ µs ASOOH*, while from 215 µs ASOOH*, the flame tip moved out of the visualization zone. This figure confirms the flame is stabilized at 430 µs ASOOH* with a constant lift-off length until 1 ms ASOI, which is the window time we focus on here (see [5] for more details).

Instantaneous and averaged OH* images at 850 K, $\rho_{inj} = 21.6$ kg/m^3 are reported respectively in Figures 15 and 16. Image processing is the same as above: instantaneous images are filtered using a median and then a Gaussian filter, each of them using a five pixel window size. Averages are calculated from raw images, based on 20 experiments. The behavior at 850 K is similar to that at 900 K, and the flame is stabilized at 430 µs for the both temperatures. Nevertheless, ignition kernels appear further downstream the injector in comparison to the higher temperature case. As expected, the lift-off length is larger at 850 K [5], which is confirmed on the average images reported in Figure 16. These average fields confirm the early stages of the ignition process occur further downstream the injector at this lower temperature, which is consistent with the larger formaldehyde penetration of 43 mm at 614 µs ASOI.

In order to study the variability of the ignition location, the average and RMS of OH* chemiluminescence images are reported in Figure 17 at the onset of hot ignition.

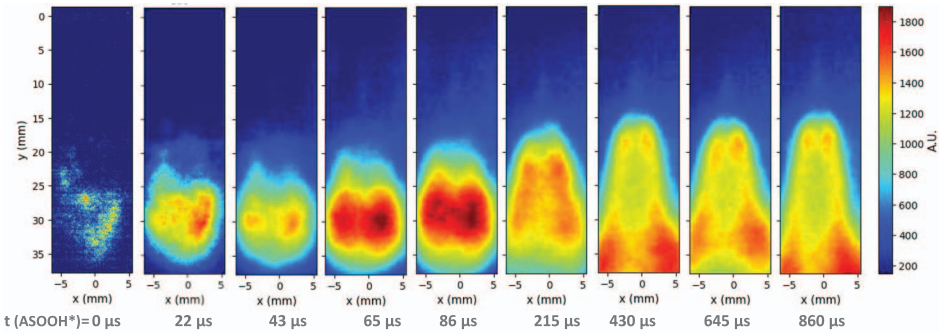

Fig. 14. Average of raw OH* images during a spray A autoignition experiment at $T_{\text{inj}} = 900$ K, $\rho_{\text{inj}} = 21.3$ kg/m^3. Average calculated over 41 experiments.

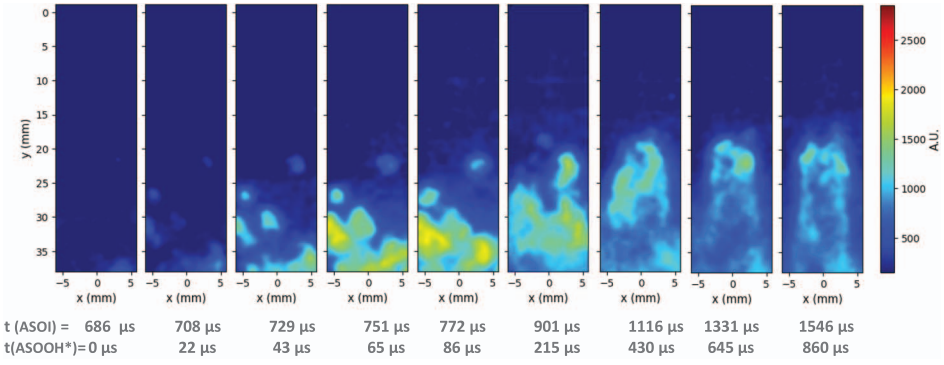

Fig. 15. Filtered instantaneous OH* images during a spray A autoignition experiment at $T_{\text{inj}} = 850$ K, $\rho_{\text{inj}} = 21.6$ kg/m^3.

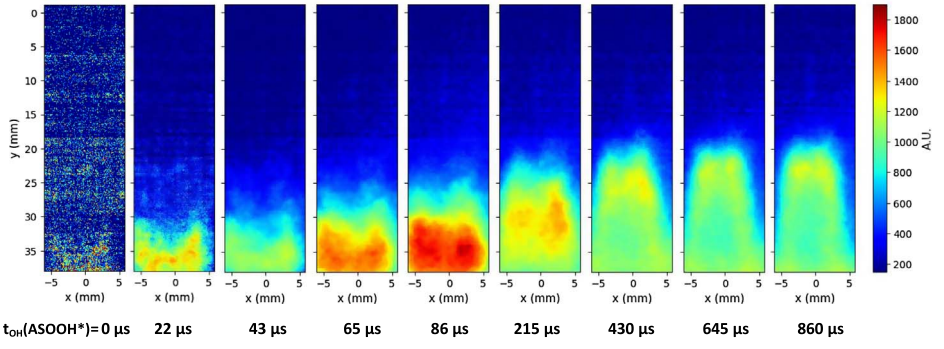

Fig. 16. Average of raw OH* images during a spray A autoignition experiment at $T_{\text{inj}} = 850$ K, $\rho_{\text{inj}} = 21.6$ kg/m^3. Average calculated over 20 experiments.

In an attempt to mitigate the jitter of hydraulic delay, time is normalized by the onset of OH* emission for the RCM data. The RMS and average fields display similar distributions: high RMS levels are found both inside and at the periphery of the region corresponding to the average OH* emission. The same observation can be made from the OH* images of Wright *et al.* recorded 2500 µs after the start of injection for a *n*-heptane spray [9]. In the both cases, the high RMS levels result from the stochastic nature of ignition, with a large contribution issued from the variations of the ignition location. In the RCM, the RMS field also reveals a very few ignition events occur closer to the injector, at 15 mm from the tip. It is worth noticing the residual flow is very weak (average velocity $U < 0.3$ m/s) in the RCM at SOI [6]. Consequently, it does not induce any additional fluctuation to the ignition process, which would not be the case in a diesel engine [9]. Besides, the experiment of Wright *et al.* [9] was also designed to provide reproducible conditions for the spray ignition. For the both studies, larger kernels in instantaneous images often display higher levels of OH* emission. Therefore the average and RMS fields are affected by the OH* intensity level: they do not perfectly represent the probability of occurrence of the first kernels.

In order to obtain more quantitative data on the position of the first OH* kernels, a statistical approach is used

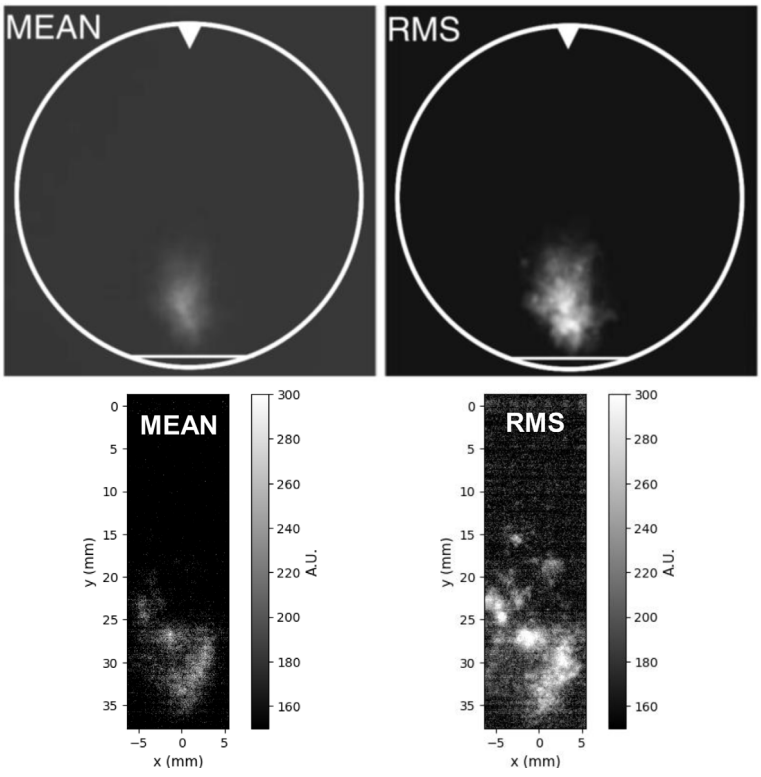

Fig. 17. OH* chemiluminescence at the time of ignition: average and RMS values. Images computed from 48 individual realizations 2.5 ms after SOI in a *n*-heptane spray [9] with permissions of *Springer* (top). Images obtained at 900 K in the present work from 51 individual realizations at $t = 0$ µs ASOOH* (bottom).

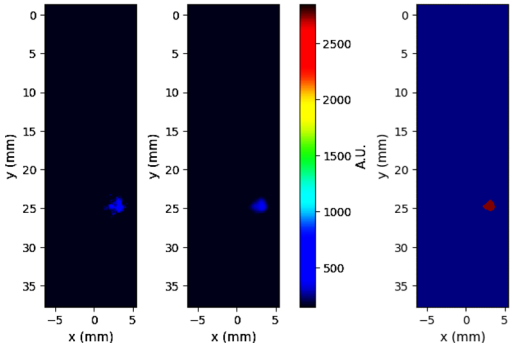

Fig. 18. Intermediate steps for probability of OH* ignition. Left: raw image, middle: filtered image, right: binarized image.

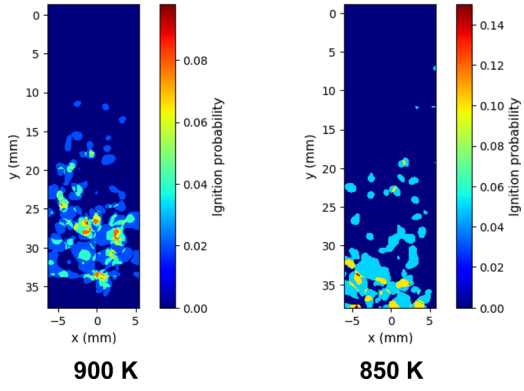

Fig. 19. Probability of ignition at a given position at $t_{\mathrm{inj}} = 900$ K and 850 K, respectively $\rho_{\mathrm{inj}} = 21.3$ kg/m^3 and 21.6 kg/m^3. Statistics are based on the first image corresponding to the OH* kernel(s) appearance ($t = 0$ µs ASOOH*). Respectively calculated over 51 and 20 experiments.

for the both temperatures: the image corresponding to the first OH* kernel is filtered and binarized, using the parameters reported above (see Fig. 18). The arithmetic mean of binarized images is calculated over the dataset (see Fig. 19). This quantity represents the OH* ignition probability map, e.g. the probability of presence of the first OH* kernels – e.g. at $t_{\mathrm{ASOOH}^*} = 0$ µs – at one given location. Of course, a very large number of experiments would be needed to obtain fully converged probability fields, because the first kernel is small and also as the very onset of ignition phenomenon displays a high level of stochasticity. Nevertheless, these data are found significant as they provide clear trends, with a well-defined procedure. This method avoids the bias on the probability that would be induced by the difference of OH* intensity between kernels of different sizes. Two different regions can be distinguished in Figure 19: most of the ignition kernels are located in the first region close to the spray head, between 25 mm and 35 mm from the injector at 900 K (resp. $y > 32$ mm at 850 K). OH* kernels sometimes appear in a second region closer to the injector, at

$11 < y < 25$ mm for a temperature of 900 K (resp. $18 < y < 32$ mm at 850 K), with a lower probability. This highlights the high variability in the location of the hot ignition process. The hot ignition kernels are observed in the whole vapor region, which corresponds to the formaldehyde region a few microseconds before the onset of hot ignition. The higher probability observed at $25 < y < 35$ mm suggests the reactivity is higher reactivity at these abscissa. This is consistent with the fact, (i) fluid particles located in this region were subjected to a higher residence time and thus a larger mixing duration and (ii) the range of equivalence ratio in this region includes favorable conditions, for instance slightly rich mixtures may lead to shorter ignition delays. The present results provide useful statistical data of the onset of spray A ignition. This would be particularly difficult to obtain from numerical computations, as running one hundred of LES computations of spray ignition would lead to very high computational costs.

4 Conclusion

Temporal characterization of spray A ignition was performed in the optical RCM of *Pprime Institute* using simultaneous high-speed OH* chemiluminescence and two-pulse formaldehyde PLIF. Two different temperatures are considered at SOI: 900 K and 850 K. The results complement existing spray A studies: they provide additional data on the time evolution and the repeatability of the early stages of both cool flame and hot ignition phenomena, and on the temporal evolution of the CH_2O region in between. The latter represents a key novelty of the present work. Two-pulse PLIF images show the development of several kernels at the onset of formaldehyde appearance. Shortly after this phase, the cool flame region expands at high velocity around the kernels and further downstream towards the rich region at the spray head, reaching finally most of the vapor region. In terms of phenomenology, the onset of low temperature ignition is similar to that described in several DNS studies in canonical jet configurations representative of the spray A. Regarding the specific spray A configuration, our observations support the existence of a cool reaction wave in the vapor phase as suggested by Dahms *et al.* [20]. In particular, for some cases, formaldehyde region propagates fast in the vapor toward the spray head, but low levels of formaldehyde signal are also observed very early at the jet head. This element does not confirm or infirm the role of diffusion or the contribution of the turbulent transport in the cool flame propagation evoked in the literature [20, 23]. Nevertheless, (i) it is clear vapor stratification affects this propagation, (ii) the time scale related to formaldehyde production – the cool flame excitation time – is of the same magnitude order as that of the cool flame expansion to the whole vapor region. Our results confirm that once formaldehyde has expanded over most of the vapor phase, formaldehyde is convected downstream according to the vapor penetration process. Shortly after this phase, OH* images show high temperature ignition occurs in one or several small kernels, formaldehyde being consumed in this region. The fast growth of the OH* kernels suggests autoignition plays a prominent role at the onset of the propagation process. The results evidence the stochasticity of the early stages of hot ignition, and statistics are provided about the location of the first OH* kernels. The subsequent growth of hot OH* regions both upstream and downstream is characterized as well, and instantaneous and average data are provided on this transient phase leading to the flame stabilization. In conclusion, the time-resolved data reported here provide further insights into the ignition dynamics of the spray A and contribute to the knowledge of the underlying mechanisms. These results will be useful for future validation and improvement of numerical models of spray A ignition, and more generally for the modeling of diesel spray ignition.

Acknowledgments. The authors acknowledge the *National Research Agency* (contract ANR-14-CE22-0015-01) for financial support to the ECN-France project. Alain Claverie is acknowledged for providing assistance for the implementation and use of optical diagnostics.

References

1 Engine Combustion Network, https://ecn.sandia.gov/.
2 Pickett L., Genzale C., Bruneaux G., Malbec L.M., Hermant L., Christiansen C., Schramm J. (2010) Comparison of diesel spray combustion in different high-temperature, high-pressure facilities, *SAE Int. J. Engines* **3**, 2, 156–181.
3 Bardi M., Payri R., Malbec L.M., Bruneaux G., Pickett L.M., Manin J., Bazyn T., Genzale C. (2012) Engine Combustion Network: Comparison of spray development, vaporization and combustion in different combustion vessels, *Atomization Spray* **22**, 10, 807–842.
4 Bardi M., Bruneaux G., Malbec L.-M. (2016) *Study of ECN injectors' behavior repeatability with focus on aging effect and soot fluctuations*, SAE Technical Papers 2016-01-0845.
5 Hespel C., Ben Houidi M., Ajrouche H., Foucher F., Haidous Y., Moreau B., Nilaphai O., Rousselle C., Bellenoue M., Claverie A., Sotton J., Strozzi C., Bardi M., Bruneaux G., Malbec L.-M. Characterization of the ECN spray A in different facilities. Part 2: Spray vaporization and combustion, *Oil Gas Sci. Technol. - Rev. IFP Energies nouvelles.* Article submitted.
6 Ben Houidi M., Hespel C., Bardi M., Nilaphai O., Malbec L.-M., Sotton J., Bellenoue M., Strozzi C., Ajrouche H., Foucher F., Moreau B., Rousselle C., Bruneaux G. (2020) Characterization of the ECN spray A in different facilities. Part 1: boundary conditions characterization, *Oil Gas Sci. Technol. - Rev. IFP Energies nouvelles* **75**, 35. doi: 10.2516/ogst/2020023.
7 Maes N., Meijer M., Dam N., Somers B., Baya Toda H., Bruneaux G., Skeen S.A., Pickett L.M., Manin J. (2016) Characterization of spray A flame structure for parametric variations in ECN constant-volume vessels using chemiluminescence and laser-induced fluorescence, *Combust. Flame* **174**, 138–151.
8 Idicheria C.A., Pickett L.M. (2007) *Quantitative mixing measurements in a vaporizing diesel spray by Rayleigh imaging*, SAE Technical Paper 2007–01-0647.

9 Wright Y.M., Margari O.-N., Boulouchos K., De Paola G., Mastorakos E. (2010) Experiments and simulations of n-heptane spray auto-ignition in a closed combustion chamber at diesel engine conditions, *Flow Turb. Combust.* **84**, 49–78.

10 Baritaud T.A., Heinze T.A., Le Coz J.F. (1994) *Spray and self-ignition visualization in a DI diesel engine*, SAE Technical Paper 940681.

11 Liao C., Terao K. (1995) A statistical investigation of ignition in a fuel spray using a shock tube. JSME, *Int. J. Ser. B* **38**, 136–142.

12 Mastorakos E., Baritaud T.A., Poinsot T.J. (1997) Numerical simulation of autoignition in turbulent mixing flows, *Combust. Flame* **109**, 198–223.

13 Hilbert R., Thévenin D. (2002) Autoignition of turbulent non-premixed flames investigated using direct numerical simulation, *Combust. Flame* **128**, 22–37.

14 Mastorakos E. (2009) Ignition of turbulent non-premixed flames, *Prog. Energy Combust. Sci.* **35**, 57–97.

15 Aggarwal S.K. (1998) A review of spray ignition phenomena: Present status and future research, *Prog. Energy Combust. Sci.* **24**, 6, 565–600.

16 Tagliante F., Malbec L.-M., Bruneaux G., Pickett L.M., Angelberger C. (2018) Experimental study of the stabilization mechanism of a lifted diesel-type flame using combined optical diagnostics and laser-induced plasma ignition, *Combust. Flame* **197**, 215–226.

17 Tagliante F., Poinsot T., Pickett L.M., Pepiot P., Malbec L.-M., Bruneaux G., Angelberger C. (2019) A conceptual model of the flame stabilization mechanisms for a lifted Diesel-type flame based on direct numerical simulation and experiments, *Combust. Flame* **201**, 65–77.

18 Dalakoti D.K., Savard B., Hawkes E.R., Wehrfritz A., Wang H., Day M.S., Bell J.B. (2020) Direct numerical simulation of a spatially developing n-dodecane jet flame under Spray A thermochemical conditions: Flame structure and stabilisation mechanism, *Combust. Flame* **217**, 57–76.

19 Skeen A.S., Manin J., Pickett L.M. (2015) Simultaneous formaldehyde PLIF and high-speed schlieren imaging for ignition visualization in high-pressure spray flames, *Proc. Combust. Inst.* **35**, 3167–3174.

20 Dahms R.N., Paczko G.A., Skeen S.A., Pickett L.M. (2017) Understanding the ignition mechanism of high-pressure spray flames, *Proc. Combust. Inst.* **36**, 2, 2615–2623.

21 Krisman A., Hawkes E.R., Talei M., Bhagatwala A., Chen J.H. (2015) Polybrachial structures in dimethyl ether edge-flames at negative temperature coefficient conditions, *Proc. Combust. Inst.* **35**, 999–1006.

22 Krisman A., Hawkes E.R., Talei M., Bhagatwala A., Chen J.H. (2017) A direct numerical simulation of cool-flame affected autoignition in diesel engine-relevant conditions, *Proc. Combust. Inst.* **36**, 3567–3575.

23 Borghesi G., Krisman A., Lu T., Chen J.H. (2018) Direct numerical simulation of a temporally evolving air/n-dodecane jet at low-temperature diesel-relevant conditions, *Combust. Flame* **195**, 183–202.

24 Krisman A., Hawkes E.R., Chen J.H. (2019) A parametric study of ignition dynamics at ECN spray A thermochemical conditions using 2D DNS, *Proc. Combust. Inst.* **37**, 4787–4795.

25 Ju Y., Reuter C.B., Yehia O.R., Farouk T.I., Won S.H. (2019) Dynamics of cool flames, *Prog. Energy Combust. Sci.* **75**, 100787.

26 Strozzi C., Claverie A., Prevost V., Sotton J., Bellenoue M. (2019) HCCI and SICI combustion modes analysis with simultaneous PLIF imaging of formaldehyde and high-speed chemiluminescence in a rapid compression machine, *Combust. Flame* **202**, 58–77.

27 Bakker P.C., Maes N., Dam N. (2017) The potential of on- and off-resonant formaldehyde imaging combined with bootstrapping in diesel sprays, *Combust. Flame* **182**, 20–27.

28 ECN6 Proceedings. (2018) Oral presentation, flame structure topic, in: *6th workshop of the Engine Combustion Network, ECN6, 10–11 September, 2018*, Universitat Politecnica de Valencia, Spain. https://ecn.sandia.gov/ecn-workshop/ecn6-workshop.

29 Pei Y., Som S., Pomraning E., Senecal P.K., Skeen S.A., Manin J., Pickett L.M. (2015) Large eddy simulation of a reacting spray flame with multiple realizations under compression ignition engine conditions, *Combust. Flame* **162**, 4442–4455.

30 Engine Combustion Network. https://ecn.sandia.gov/schlieren-code/.

31 Nicoli C., Clavin P., Liñan A. (1990) Travelling waves in the cool flame regime, in: Gray P., Universite libre de Bruxelles, University of Leeds, Commission of the European Communities (eds), Spatial inhomogeneities and transient behavior in chemical kinetics, Proceedings in Nonlinear Science, Manchester University Press, Manchester, UK, pp. 317–334.

32 Quintens H., Bellenoue M., Strozzi C., Zitoun R. (2019) Deflagration/autoignition/detonation transition induced by flame propagation in a n-decane/O_2/Ar mixture, *Flow Turb. Combust.* **102**, 3, 735–755.

33 Markides C.N., Mastorakos E. (2008) Flame propagation following the autoignition of axisymmetric hydrogen, acetylene and normal-heptane plumes in turbulent coflows of hot air, *J. Eng. Gas Turb. Power* **130**, 011502.

Appendix

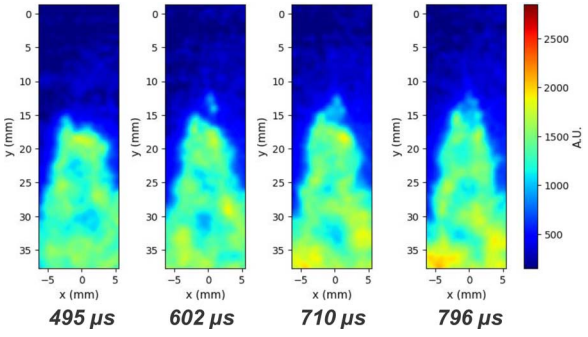

Fig. A1. Filtered instantaneous OH* images during a spray A autoignition experiment at $T_{inj} = 900$ K, $\rho_{inj} = 21.3$ kg/m^3. The ignition kernel upstream at $t = 602$ µs ASOOH* shows the autoignition mechanism participates to the flame stabilization.